

## Article

# Automatic Method of Exploring the Landscape of Freeform Dioptric Optical Problems, Working in the Infrared Region

Thibaut Mayeur<sup>1,2,3,\*</sup> , Jean-Baptiste Volatier<sup>1</sup>, Guillaume Druart<sup>1</sup>, Françoise Cau<sup>2</sup>, Elodie Tartas<sup>3</sup> and Alain Durand<sup>3</sup>

<sup>1</sup> ONERA, 6 Chemin de la Vauve aux Granges, 91120 Palaiseau, France; guillaume.druart@onera.fr

<sup>2</sup> Safran Electronics & Defense, 100 Avenue de Paris, 91300 Massy, France

<sup>3</sup> Lynred, 364 Route de Valence, 38113 Veurey-Voroize, France

\* Correspondence: thibaut.mayeur@onera.fr

**Abstract:** We present an automated method of finding different freeform dioptric starting systems, working in the infrared region, for further optimization in commercial optical design software. Our developed method couples the simultaneous multiple surface (SMS) method, introduced by Benítez and Miñano, with automatic optimization in Zemax OpticStudio. The method allows an optical designer to explore the merit function (MF) landscape of freeform optical problems. In this article, we apply our method to a size, weight, and power (SWaP) problem, and we compare our designed system with a system found in the literature that has the same aperture of F/1.2. Then, we increase the aperture of the system up to F/0.9, taking advantage of the use of freeform surfaces.

**Keywords:** freeform optics; optical design; global optimization method; simultaneous multiple surface method



**Citation:** Mayeur, T.; Volatier, J.-B.; Druart, G.; Cau, F.; Tartas, E.; Durand, A. Automatic Method of Exploring the Landscape of Freeform Dioptric Optical Problems, Working in the Infrared Region. *Optics* **2023**, *4*, 482–499. <https://doi.org/10.3390/opt4030035>

Academic Editor: Feruz Ganikhanov

Received: 12 May 2023

Revised: 30 June 2023

Accepted: 11 July 2023

Published: 1 August 2023



**Copyright:** © 2023 by the authors. Licensee MDPI, Basel, Switzerland. This article is an open access article distributed under the terms and conditions of the Creative Commons Attribution (CC BY) license (<https://creativecommons.org/licenses/by/4.0/>).

## 1. Introduction

Since its inception, the design of optical imaging systems has relied on spherical surfaces and, later on, rotationally symmetric surfaces, such as spheres, conics, aspheres, etc. However, in the 1970s, the first optical system with a surface without rotational symmetry was commercialized [1]. In this article, “freeform surface” refers to surfaces without rotational symmetry [2]. An optical design always aims to find an optimum between conflicting requirements. For example, in many fields of application (space, defense, and automotive industries), both optical performance and the minimization of volume are essential. By bringing more degrees of freedom to the designer, freeform systems can out-compete classical systems in all requirements. For example, the literature has shown that off-axis catoptric freeform systems achieve a volume reduction of 39% for a similar optical quality [3]. Therefore, a freeform system often improves classical designs, such as the three-mirror anastigmat (TMA) design [2,3].

However, a freeform surface brings new challenges to optical design. The use of freeform optics makes optimizing the merit function more complex, due to the large number of degrees of freedom. In turn, the final results will depend on the designer’s know-how even more than in classical systems. Indeed, an experienced optical designer will often choose a better starting point for optimization than an inexperienced one. Most of the time, lens design software uses a local optimization algorithm, which is why the starting point is so important, to obtain an excellent optical system.

New design methods have appeared in recent decades, to handle and simplify this problem, generating starting points from scratch. We can sort them into two categories: deep learning methods and direct construction based on ray tracing. In deep learning methods, various studies have been published [4–7], demonstrating promising results. Nevertheless, the need for relevant and numerous data to correctly train a neural network is a significant bottleneck in optical design, especially in freeform optical design, where data are

limited. In direct construction methods of interest, we can single out the SMS method [8–19], the point-by-point method [20,21], and differential ray tracing methods [22–25]. Between these different methods, we decided to use the SMS method as our automated method. We chose this method as it requires few initial hypotheses about the system. The second point is that this method treats surfaces independently, enabling a solution to the problem without any approximation, and allowing for the construction of wide field-of-view (FOV) freeform systems with a low F-number. By contrast, surfaces are treated dependently in differential ray tracing methods, making the problem harder to solve. Consequently, differential methods allow either the construction of low F-number systems or wide FOV systems, but not both. Moreover, most of the differential methods cannot construct systems with more than two surfaces, except the “First Time Right” method [26].

Here, we describe our global approach, developed based on our implementation of the SMS-3S-3D method. In this method, we use the SMS-3S-3D algorithm as a generator of freeform systems, and we couple it with automatic optimization in Zemax. This method allows for obtaining various freeform starting configurations with good optical quality over the whole FOV, and not only on specific fields, as is the case for systems resulting from the standard SMS method. This method uses few initial hypotheses about the systems, and it does not require advanced knowledge in optical design. We used this method to increase the aperture of an existing SWaP two-lens system designed for the European Project tHERmal vIsion AUgmented awarenesS, passing from an F-number of 1.2 to 0.9, which is complex, using only two lenses [27]. During the design of the SWaP infrared wide FOV system, we observed that using an inverse thick meniscus in two-lens infrared systems was sufficient to correct the Petzval curvature and that the use of a field flattener lens was not the best solution in this case, as it increased the local aperture of the front lens.

In this article, we will first describe the implementation of the SMS-3S-3D method used in our automated method. Then, we will depict the developed automated method, to explore the landscape of an optical merit function (MF) for dioptric problems in the infrared region. This method can handle the exploration of optical problems with up to three freeform surfaces and one user-defined surface. Using this method, we found different starting configurations for further optimization in commercial optical design software.

## 2. Material and Methods

### 2.1. General Principle of the SMS Method

The SMS method is a generalization of the Cartesian oval principle to multiple surfaces. A Cartesian oval is an optical surface reflective or refractive that couples an incident wavefront into an outgoing one. Figure 1 illustrates the difference between a spherical surface and an imaging Cartesian oval, both imaging the on-axis field. The image obtained through the spherical surface is blurred, whereas the image obtained through the Cartesian oval is perfect. For imaging a field through an imaging Cartesian oval, there are two options: we can either set the optical path length or directly specify the image coordinates. In our SMS algorithms, we use the image coordinate criteria.

The SMS-3S-3D method constructs a system of three surfaces (3 Cartesian ovals) with 3 aberration-free fields. In our case, we perform the SMS-3S-3D method to construct two air-spaced lenses. Therefore, we must add one known surface to the system, before performing the SMS-3S-3D method. We defined the fourth surface plane in our current implementation of the SMS-3S-3D method. This choice was arbitrary, and could have been any surface of the system and any surface representation, as long as it was defined. To perform the SMS-3S-3D method, we have to set the following initial settings:

- Studied fields ( $\theta_0$ ,  $\theta_1$ , and  $\theta_2$ );
- F-number ( $F/\#_{target}$ );
- Focal length;
- Refractive indices;
- Position of the image plane;
- Central curved radii of surfaces 1 and 2 ( $R_1$  and  $R_2$ );
- Thicknesses between all surface vertices.

Here, we will explain our implementation of the SMS-3S-3D method based on M. Nikolić's implementation [9].

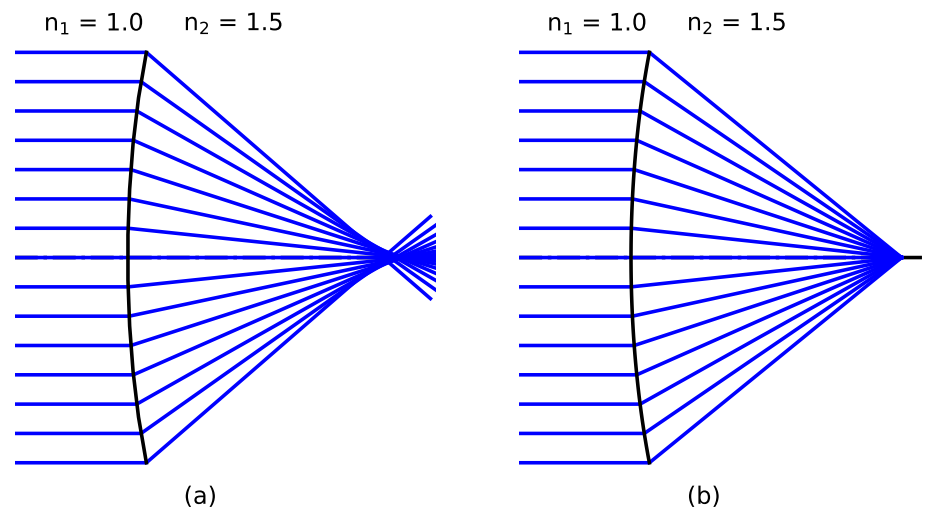


**Figure 1.** (a) Spherical surface; (b) Cartesian oval imaging the on-axis field.

## 2.2. Explanation of the SMS Method Applied to 3 Surfaces in 3D (SMS-3S-3D)

The SMS-3S-3D method encompasses two phases: Phases 1 and 2. Phase 1 generates the initial system,  $Syst_0$ , from the settings. It is extended by Phase 2, to obtain the optical system with the targeted F-number. We call SMS systems, noted  $Syst_{SMS}$ , systems resulting from an SMS method. The two phases are described in the thesis of M. Nikolić [9]. We will describe how we implement them, which may differ from the way of M. Nikolić, as we had only a few insights into their implementation of the SMS-3S-3D method, as their implementation was unavailable.

### 2.2.1. Explanation of Phase 1

At the beginning of Phase 1, we have no information about surface 3, except its vertex position. Figure 2 illustrates the optical system, using only the information of the settings. Therefore, the aims of Phase 1 are to construct the central part of surface 3, delimit the central part of surface 1, and determine the size of the central curve of surface 2. The central curve of a surface refers to the curve contained in the XZ plane. The last remaining aim of Phase 1 is to approximate surfaces 1 and 3 into non-uniform rational basis spline (NURBS) surfaces, using the NURBS surface approximation algorithm called the Cubic Local Patch (CLP) algorithm [8].

To achieve this, we split Phase 1 into four steps:

1. Computation of the central curve of surface 3,  $C_1^3$ : We propagate rays from field  $\theta_1 = 0^\circ$  through the central curve of surfaces 1 and 2. The size of the central curve of surface 1 is defined by  $F/\#_{targeted}$ , as surface 1 is set as the pupil of our SMS system. This imposes the size of the central curve of surface 2. Then, using the Cartesian oval principle, we compute the central curve of surface 3, such that the rays are focused on  $Im_1$  after their propagation through the central curve of surfaces 3 and 4. This step is shown in Figure 3a.

2. Computation of the upper curve of surface 3,  $C_0^3$ : We propagate rays from field  $\theta_0 = \theta_{max}$  through the lower curve of surface 1 and the central curve of surface 2. The lower curve of surface 1 is the curve of surface 1 that refracts rays of field  $\theta_0$  onto the central curve of surface 2. Then, using the Cartesian oval principle again, we compute the upper curve of surface 3, such that the rays are focused on  $Im_0$ . This step is shown in Figure 3b.
3. Computation of the lower curve of surface 3,  $C_2^3$ : We compute by symmetry the lower curve of surface 3. We can perform this thanks to the symmetry of the problem (symmetry of fields and surfaces with respect to the XZ plane). Otherwise, it is possible to compute this curve in the same manner as step 2, by substituting  $\theta_0$  and  $Im_0$  with  $\theta_2 = -\theta_{max}$  and  $Im_2$ . This step is shown in Figure 3c.
4. Approximation of surfaces 1 and 3 into NURBS surfaces: Using the CLP algorithm, we approximate surfaces 1 and 3 into NURBS surfaces.

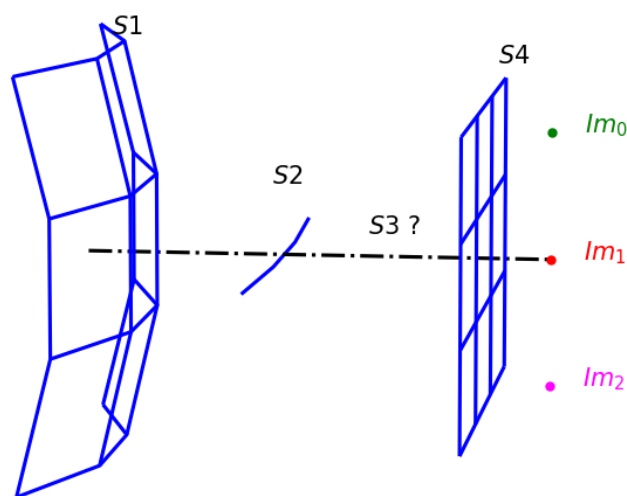


**Figure 2.** Example of an initial system constructed from the settings of the SMS-3S-3D method. Surfaces 1 and 2 are described using their spherical parts close to the optical axis defined by the radii,  $R_1$  and  $R_2$ . At this point, we have no information about surface 3, except its vertex position. Finally, surface 4 is defined as a plane.

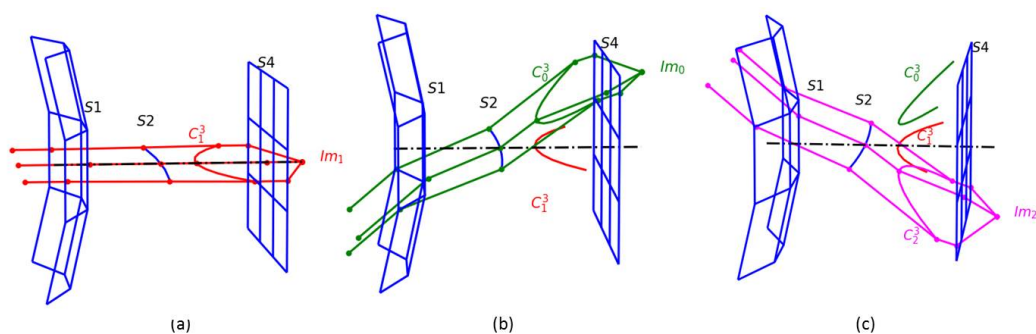


**Figure 3.** Scheme of (a) Step 1, which allows the computation of the central curve of surface 3, using the on-axis field, (b) Step 2, which allows the computation of the upper curve of surface 3, using the field  $\theta_{max}$ , and (c) Step 3, which is the same symmetrical step of Step 2, allowing the computation of the lower curve of surface 3.

As a result of the above four steps, we obtain the initial system,  $Syst_0$ , to begin Phase 2. Figure 4 shows an example of  $Syst_0$ .

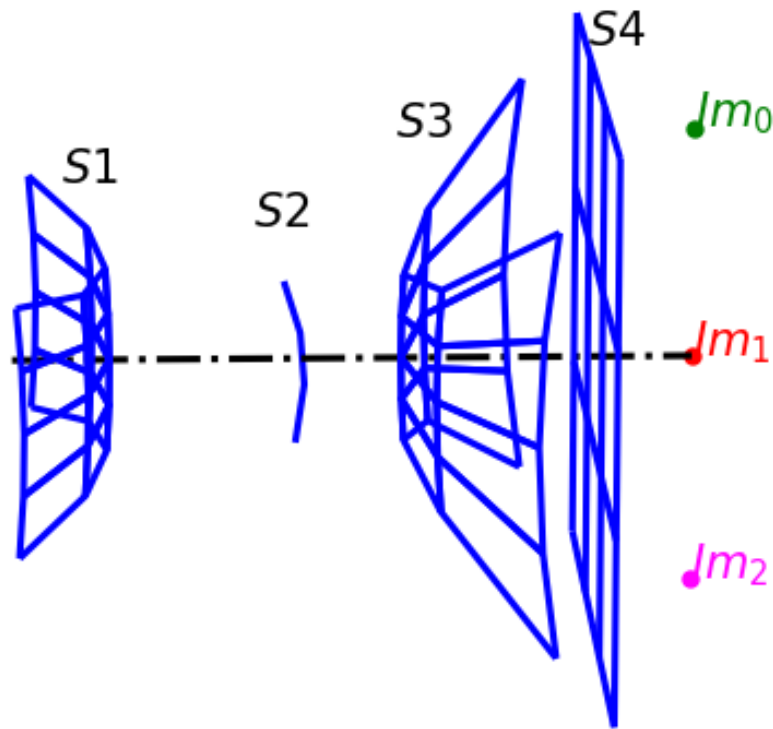


**Figure 4.** Layout of the central parts close to the optical axis of surfaces 1, 2, and 3, computed during Phase 1. Surfaces 1 and 3 are plotted after their approximation into the NURBS surfaces. This layout illustrates a system,  $Syst_0$ , at the output of Phase 1.

2.2.2. Explanation of Phase 2

Phase 2 constructs the optical system with the required F-number from the starting system,  $Syst_0$ , by progressively extending each surface and applying the principle of SMS extension [9,10]. The principle of SMS extension for the SMS-3S-3D method consists of propagating rays through the system, passing by three known surfaces and one unknown part of the remaining surface.

Before extending the surfaces, we must associate each surface with the field, allowing the extension of each one. The associations made for our study are written in Table 1.

**Table 1.** Association between surface and field for the extension of the system.

Surface	Associated Field
S1	$\theta_0 = \theta_{max}$
S2	$\theta_1 = 0^\circ$
S3	$\theta_2 = -\theta_{max}$

The first step is to extend surface 2, as we only know its central curve. Therefore, we cannot extend any other surface than this one. We use the first extension of surface 2 as an example of the SMS extension principle, so we will not detail the other extensions. To extend surface 2, we propagate rays of the field,  $\theta_1$ , through an unknown part of surface 2 and known parts of surfaces 1, 3, and 4. Figure 5a shows the ray tracing that allows the computation of the point cloud defining surface 2 after the first extension. Figure 5b shows surface 2 after applying the CLP algorithm to the point cloud.

Now that we have expanded surface 2, we can begin the successive extensions of each surface, to reach the targeted F-number for the system. Finally, we obtain the SMS system noted  $Syst_{SMS}$ .

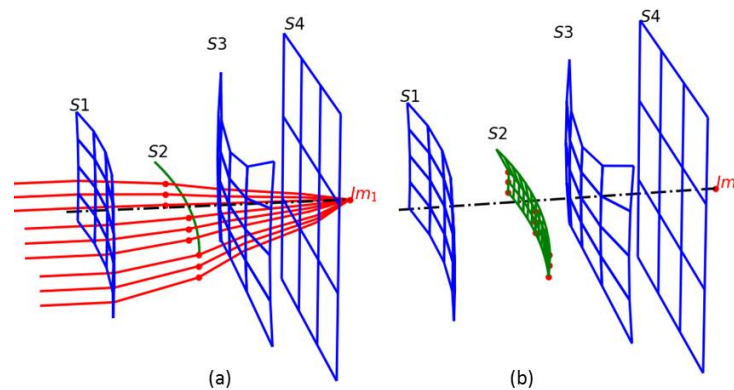


**Figure 5.** (a) Propagation of rays of field  $\theta_1$  to extend surface 2; (b) surface 2 approximated by the CLP algorithm.

### 2.3. Description of the Automated Method of Exploring the Landscape of an Optical Problem

We distinguish three parts in our automated method of exploring the landscape of optical problems. The first part consists of generating multiple freeform systems using the SMS-3S-3D method. The second part automatically optimizes the different SMS systems obtained using a standard optimization function. The third part analyzes the optical quality of the resulting systems, and classifies them into different configurations following a specific criterion.

#### 2.3.1. SMS System Generation

Before computing multiple freeform systems using the SMS-3S-3D method, we must choose the variables. For this study, we decided to vary only two variables: the radii of curvatures  $R_1$  and  $R_2$  of the front lens. We selected these two parameters as we assumed that they would have a more significant impact on the system resulting from the SMS-3S-3D method. The other parameters were kept constant. Then, we defined many sets of initial settings, to generate multiple SMS systems. The results provided us with information about the values of  $R_1$  and  $R_2$  that we needed to choose, to design an SMS system successfully.

#### 2.3.2. Automatic Optimization

For this part, we automatically optimize the SMS systems in Zemax OpticStudio. By doing this, we can find various configurations of the systems. This provides us with information about the optical MF landscape of the problem. For each optimization, we use the same nine fields contained in the upper-right part of the FOV limited by the fields  $(0^\circ, 0^\circ)$ ,  $(\theta_{x_{max}}, 0^\circ)$ ,  $(0^\circ, \theta_{y_{max}})$ , and  $(\theta_{x_{max}}, \theta_{y_{max}})$ . For this part, we need to pick a relevant ray density to optimize the fields, considering two conflicting parameters: the resulting optical quality and the computation time. Indeed, although a higher ray density used yields a higher optical quality of the system, it also results in a higher computation time. Therefore, we choose a ray density that assures a sufficient optical quality and a reasonable computation time, as we do not necessarily want to design diffraction-limited systems at this stage. We found that tracing  $16 \times 16$  rays is a good compromise.

Before performing automatic optimization, we need to fit the SMS systems on a polynomial basis, which is handled by Zemax, because SMS systems are described in NURBS. We chose to fit the surfaces onto an XY polynomial basis. We put all three freeform surface polynomial coefficients, radii of curvatures, conic coefficients, and thicknesses in variables. Automatic optimization minimizes the root-mean-square (RMS) spot size of each field, controls their centroids, and imposes constraints on the thicknesses of the systems. The most important constraint concerns the thickness of the rear lens, which needs to be less than 1 mm. Other thickness constraints limit the systems' total track and the thickness of the front lens.

### 2.3.3. Automatic Analysis and Classification of Systems

The last part of the automated method allows for the classification and analysis of the optical quality of each system. We needed to find a simple criterion for distinguishing different configurations in all the designed systems. Therefore, we decided to base our classification criterion on the best-fit sphere (BFS) sign of the surfaces of each system, so that all systems in the same configuration would have the same BFS sign for each surface. The signs (+) and (-) are associated with convex and concave surfaces, respectively. The criterion of classification is arbitrary and can easily be modified. To compare the configurations between them, we compute the mean and standard deviation of the mean value of the RMS spot radius field map of each system contained in the same configuration. These values allow us to quickly identify if one configuration is better than the others.

All the steps described previously are presented in a flowchart depicted in Figure 6.

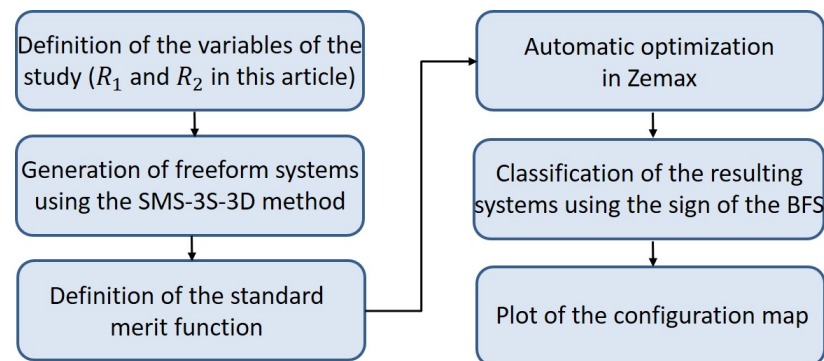


**Figure 6.** Flowchart of the automated method.

### 2.3.4. Best Systems Optimization

Once the automatic exploration of the MF landscape of the optical problem has been conducted, we select the best system of each configuration found, and we optimize them further. We note BSC(i) as the best system of configuration i. The best system of a configuration is the system that has the minimum mean RMS spot radius field map inside the same configuration. To further optimize the best systems and obtain the best possible image quality on the detector, we must change the MF. In fact, due to distortion, the initially optimized object FOV does not cover the entire detector area. To address this, we directly optimize the optical quality of the detector. In this aim, we modify the nine fields used for optimization into fields on the detector: the nine fields are contained in the upper-right part of the detector and are limited by the fields (0 mm, 0 mm), ( $X_{det}$ , 0 mm), (0 mm,  $Y_{det}$ ), and ( $X_{det}$ ,  $Y_{det}$ ). Taking the example of a  $640 \times 480$  VGA detector with a pixel pitch of  $10 \mu\text{m}$ , we have  $X_{det} = 3.2 \text{ mm}$  and  $Y_{det} = 2.4 \text{ mm}$ . As we use freeform surfaces, we must resort to large ray density to sample the surfaces correctly. Therefore, we pass from a ray density of  $16 \times 16$  to a ray density of  $200 \times 200$  for each field, to significantly improve the optical quality of the system. At this point, we will directly look at the optical quality on the detector. Thus, it might be possible that the optical quality appears worse than the optical quality before manual optimization. Nevertheless, both optical qualities are not comparable, because we are not looking at the same FOV. This phenomenon appears as we no longer look at the object FOV but directly at the FOV defined by the detector, which is larger than the initially defined object FOV, due to the negative distortion.

## 2.4. The Automated Method Applied to Monochromatic Fast Two-Lens Infrared Systems

### 2.4.1. Context and Specifications of the Study

This study aimed to design a dioptric system working in the long-wave infrared (LWIR) band, answering the SWaP problem. In optical design, the challenge of the SWaP problem is to increase the optical performance while reducing the size, mass, and cost of the system. A reduction in system size is achieved through a reduction in detector size, thereby

reducing the pixel size. However, this implies designing faster optical systems, which conflicts with size and cost reduction. In turn, we must increase the number of system variables, to increase the aperture of an optical system. This can be achieved by using more optical elements or surfaces with more degrees of freedom (DoF). Using more optical elements increases the size and cost of the system. Thus, a possibility is to use surfaces with more DoF, such as aspherical or freeform surfaces, which is now possible, thanks to recent developments in the manufacturing and testing of these complex surfaces. In this context, different studies [28,29] have been conducted, to show the benefit of using aspherical surfaces to design two-lens infrared optical systems. Considering this problem, other studies [18,30,31] have demonstrated that correcting the FOV, which perfectly matches the detector dimensions of the system, enhances the optical quality of classical systems for the same number of optical elements. Usually, on-axis classical optical systems correct the rotationally symmetric FOV defined by the diagonal of the detector and the focal length of the system. Therefore, parts of the correction are lost, due to the oversizing of the FOV compared to the dimensions of the detector. Figure 7 illustrates this phenomenon. The system must contain freeform surfaces in order to correct the FOV, so that it matches the detector perfectly, as the optical problem is no longer rotationally symmetric. This design strategy for dioptric systems is interesting in tackling the SWaP problem.

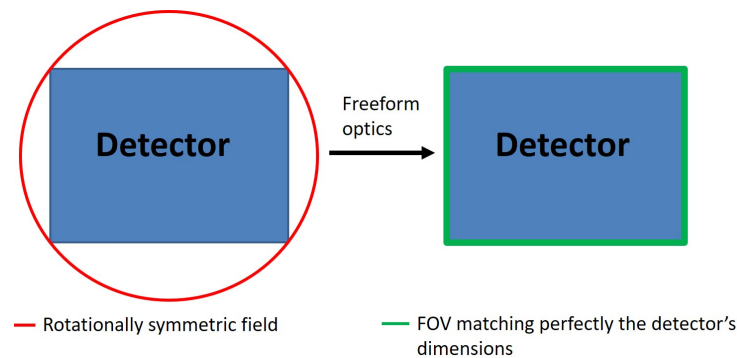


**Figure 7.** On the **left**, the rotationally symmetric FOV oversizes the dimensions of the detector. On the **right**, the FOV perfectly matches the dimensions of the detector.

In light of recent studies, where one solution to the SWaP problem is to design systems with more DoF, we developed an automatic method adapted to the SWaP problem for two-lens infrared systems. Our method can design fast and wide FOV two-lens systems with three freeform surfaces, allowing the correction of a rectangular FOV. To illustrate the relevance of our method for this type of application, we propose a comparison of our optical system, designed using the automatic method, to an optical system described in the literature [27], designed using the classical method. We chose this system as a reference system, as it works in the LWIR band, and it has been designed to answer the SWaP problem. Figure 8 depicts the layout of the system and the RMS spot radius field map.

The system is made of a front aspherical lens, in a high-index chalcogenide glass called TGG [27], and a rear lens in silicon, with a front spherical surface and a rear plane surface. The authors imposed for the silicon lens a last rear plane surface and a sag height for the front surface less than 150  $\mu\text{m}$  in their design, to maintain a low-cost approach, as it simplified its fabrication. In our study, we did not consider the sag constraint. However, we noted that the sag height of the reference system was  $-136 \mu\text{m}$ : this parameter was not a limiting operand during the optimization of the reference system, and it could be considered as a nominal solution without sag constraint. The authors also explained that, using their experiences, they started with an inverse meniscus well-known to correct the aberrations for a wide FOV system in a SWaP configuration, and they replaced the window of a microbolometer to correct the Petzval curvature of the system with a divergent plano-concave field-flattener lens [32]. Indeed, due to the decrease in pixel size, the depth of field

of the system could be insufficient to compensate for the Petzval curvature for a wide FOV. Table 2 presents the features of the reference system.

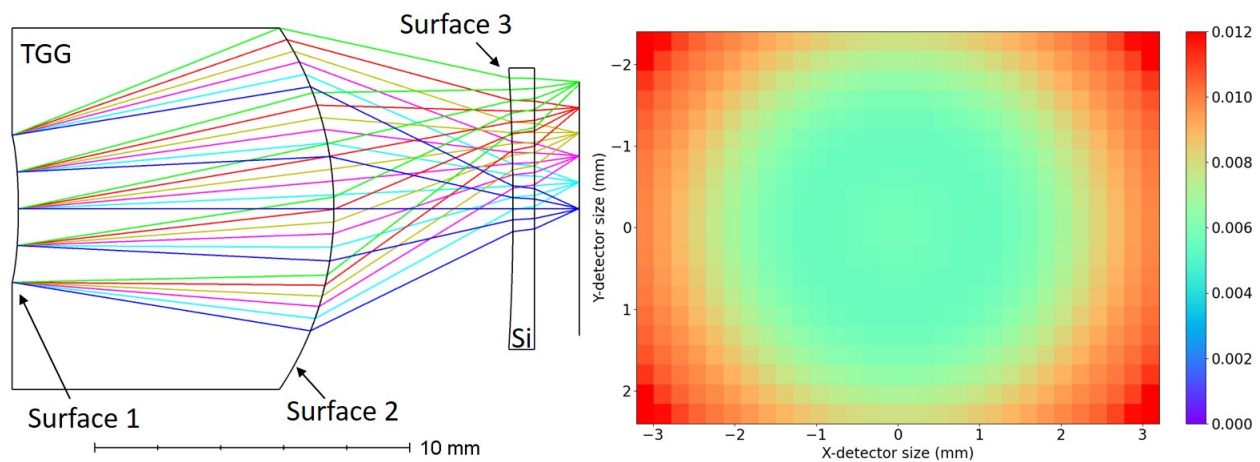


**Figure 8.** Layout and RMS spot radius field map of the reference system [27].

**Table 2.** Parameters of the reference system [27].

Parameter	Value	Parameter	Value
Focal	5.6 mm	HFOV	$\pm 34^\circ$
F/#	1.2	VGA Detector	$640 \times 480$
Pixel pitch	$10 \mu\text{m}$	Mean RMS spot radius	$7.62 \mu\text{m}$
TGG refractive index	3.39	Silicon refractive index	3.47

This study was conducted threefold. The first part consisted of designing a system with an F-number equal to 2, in order to study the effect of a reduction in the F-number on the configurations found, and to explain the results obtained, using a simple case. We also decided to make this study with a slightly higher F-number than required, as this is a standard way to design an optical system. Then, we designed a system with the same F-number (1.2) as the reference system. The second part aimed to see if we found the same configuration as the reference system, and showed that optimization over a rectangular FOV enhances the optical quality. In the last part, we took the benefit of both our automatic method and the correction of the useful FOV, to enhance the optical quality of the system by reducing its F-number. We were also interested in seeing if the best system configuration was the configuration of the reference system or another configuration found by the automated method.

For this article, we designed only monochromatic two-lens infrared systems at a reference wavelength of  $10 \mu\text{m}$ . We justified this choice by the low chromatic aberrations in the LWIR band concerning small focal length systems.

For the studies, we varied  $R_1$  and  $R_2$  between  $\pm 100 \text{ mm}$  and  $\pm 150 \text{ mm}$ , respectively. In turn, to simplify the analysis of the results, all graphics were represented according to the curvature  $1/R_1$  and  $1/R_2$ . As we took 50 values for each variable, we generated 2500 files of initial settings, where  $1/R_1$  and  $1/R_2$  varied between  $\pm 0.49 \text{ mm}^{-1}$  and  $\pm 0.33 \text{ mm}^{-1}$ , respectively.

#### 2.4.2. Study of a Monochromatic Two-Lens Infrared System with an Aperture of F/2

Applying the automated method, we found four different diffraction-limited configurations of systems. Figure 9 shows the prohibited areas of the initial parameters where no system was found (green areas). These areas could appear for two reasons. The first was that the SMS method failed to design a system with the targeted F-number. The second reason was that sometimes automatic optimization fails to optimize the system. Figure 9 also shows one principal configuration (configuration 2, with 1285 systems), two

secondary configurations (configurations 1 and 3, with 125 and 86 systems, respectively), and a last marginal configuration (with 3 systems). By looking at Figure 10, we can see that configuration 1 was made of a front convergent lens with two convex surfaces and a rear convergent lens with a front convex surface. The front surface of the front lens of configuration 2 changed to a concave surface beside configuration 1. Configuration 3 differed from configuration 1, as the front surfaces of both lenses were concave. Therefore, it was made of a front convergent lens and a divergent rear lens, such as the reference system. Despite these differences, the three configurations had a thick front lens, contrary to configuration 4, where its front lens was thin.

On the configurations map, we have marked the localization of the best system for each configuration with a cyan dot. The best systems were not optimized here, as they were already diffraction-limited on the detector. Indeed, by looking at Figure 10, we can see that the worst system, BSC(4), experienced degradation of its optical quality at the edges of the detector. Nevertheless, it had a mean RMS spot radius of  $14.97\ \mu\text{m}$ , which was inferior to the Airy spot radius of  $24.4\ \mu\text{m}$ , for an F-number of 2. We also note that the different RMS spot radius field maps are not rotationally symmetric, illustrating the freeform aspect of the designed system.

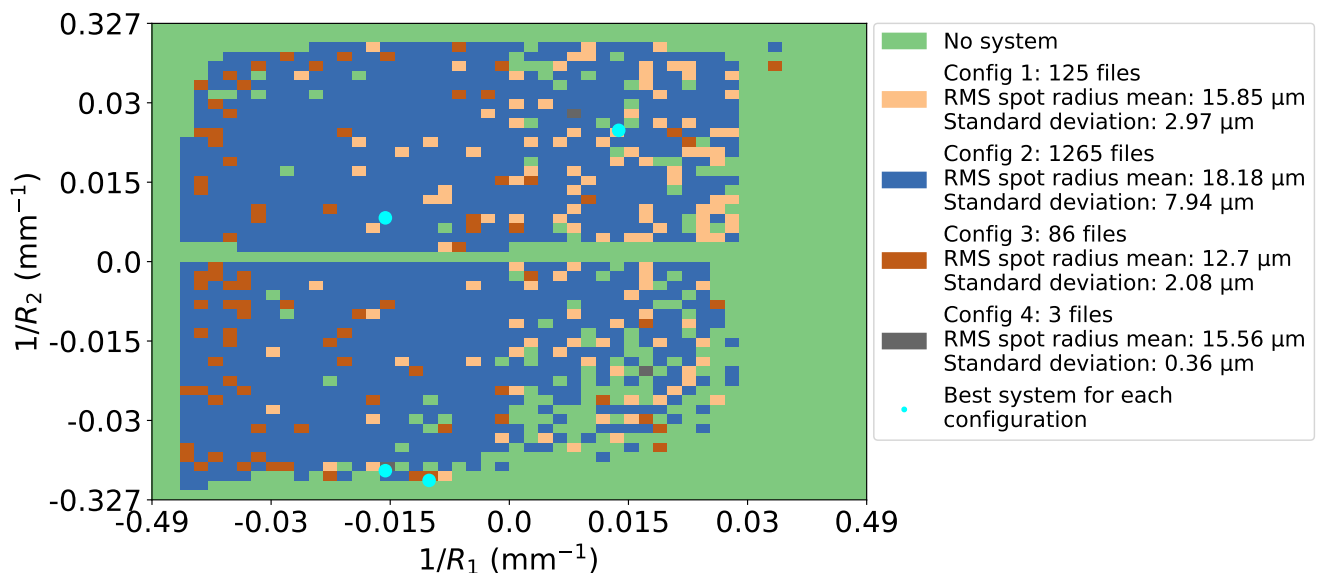


**Figure 9.** Map of the configurations found for a monochromatic two-lens infrared system with an aperture of F/2 according to  $1/R_1$  and  $1/R_2$  ( $r_{Airy} = 24.4\ \mu\text{m}$ ).

#### 2.4.3. Study of a Monochromatic Two-Lens Infrared System with an Aperture of F/1.2

We computed the map of the configurations presented in Figure 11, running the automated method for a higher aperture of F/1.2. We observed that the occupied areas by the designed systems were contained in the occupied areas of the map of the configurations of the first study (see Figure 9). Nevertheless, we designed fewer systems than during the first study. We explain this observation as a direct repercussion of the reducing F-number, as increasing the aperture for a constant FOV makes the design task harder. Another consequence is the optical quality degradation of the system, which is no longer diffraction-limited after the automated method. Indeed, by looking at Figure 12, we can see that the best system, BSC(2), had a mean RMS spot radius of  $15.48\ \mu\text{m}$ , which was superior to the Airy spot radius of  $14.64\ \mu\text{m}$ , for an F-number of 1.2. For this study, we were able to distinguish three configurations, which means that one configuration disappeared. Nevertheless, the repartition of the configurations was similar to the previous study, as we obtained one principal configuration with 671 systems, one secondary configuration with 260 systems, and one marginal configuration with only 2 systems. Figure 12 shows that the marginal configuration was the configuration of the reference system. Therefore, we found

the same configuration as the reference system using the automatic method, even though it seemed complicated to find it without experience.

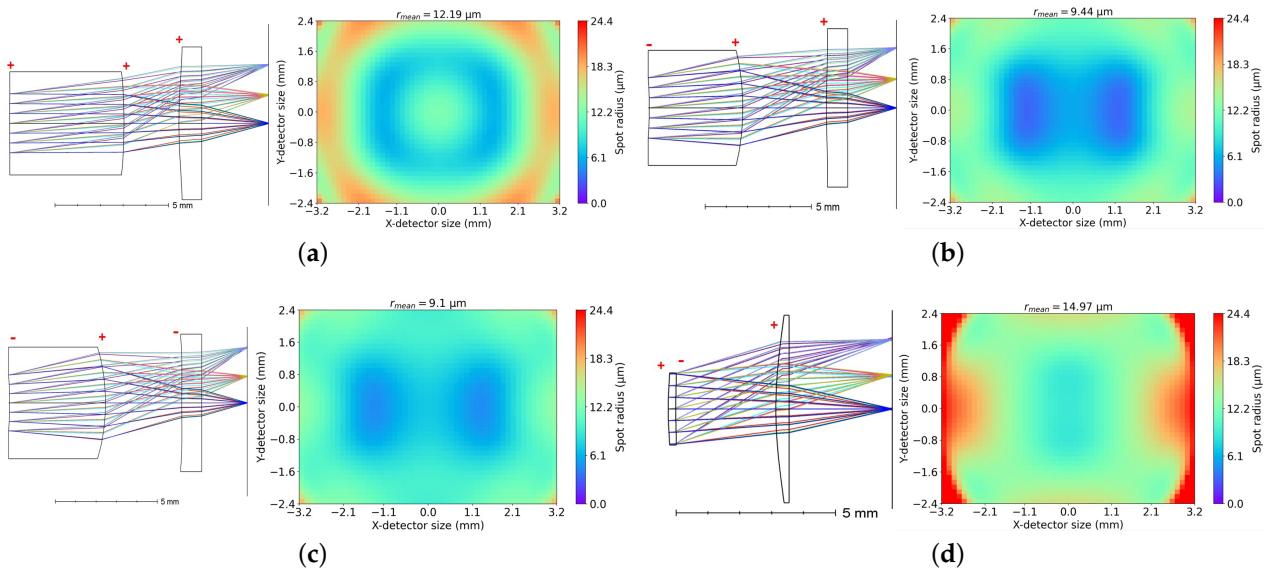


**Figure 10.** RMS spot radius field map on the same color map and layout of the best systems with an F-number of 2: (a) BSC(1) has a mean, minimum, and maximum RMS spot radius of  $r_{mean} = 12.19 \mu\text{m}$ ,  $r_{min} = 6.14 \mu\text{m}$ , and  $r_{max} = 19.84 \mu\text{m}$ ; (b) BSC(2) has a mean, minimum, and maximum RMS spot radius of  $r_{mean} = 9.44 \mu\text{m}$ ,  $r_{min} = 3.31 \mu\text{m}$ , and  $r_{max} = 18.32 \mu\text{m}$ ; (c) BSC(3) has a mean, minimum, and maximum RMS spot radius of  $r_{mean} = 9.1 \mu\text{m}$ ,  $r_{min} = 4.67 \mu\text{m}$ , and  $r_{max} = 17.58 \mu\text{m}$ ; (d) BSC(4) has a mean, minimum, and maximum RMS spot radius of  $r_{mean} = 14.97 \mu\text{m}$ ,  $r_{min} = 8.86 \mu\text{m}$ , and  $r_{max} = 55.23 \mu\text{m}$  with an F-number of 2.

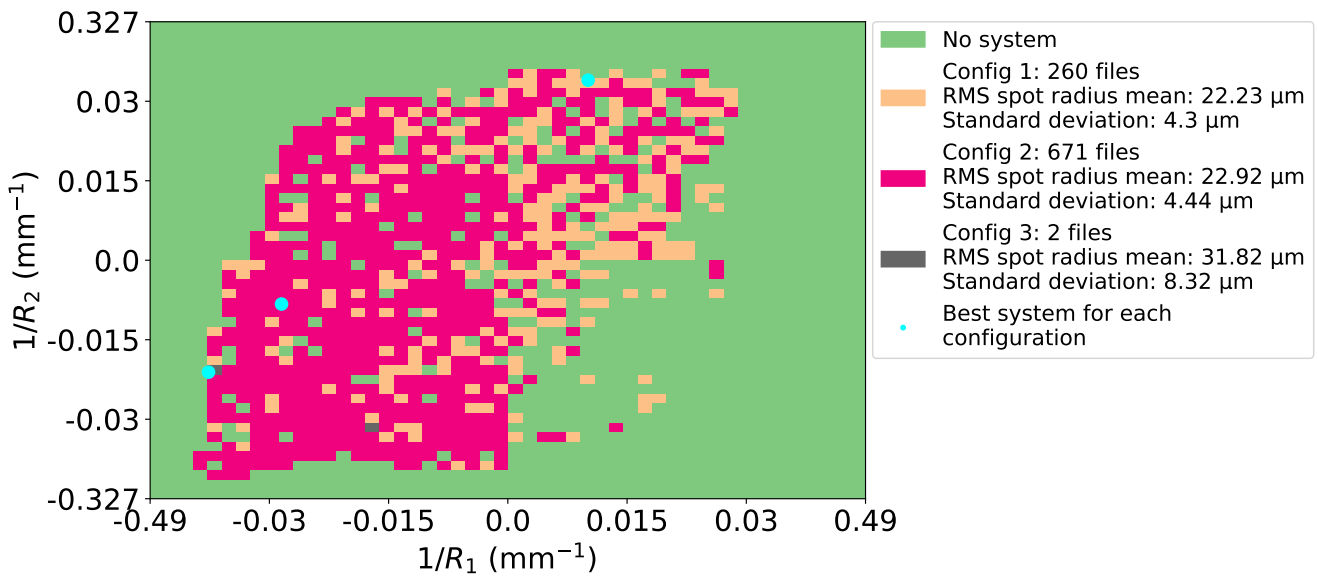


**Figure 11.** Map of the configurations found for a monochromatic two-lens infrared system with an aperture of F/1.2 according to  $1/R_1$  and  $1/R_2$  ( $r_{Airy} = 14.64 \mu\text{m}$ ).

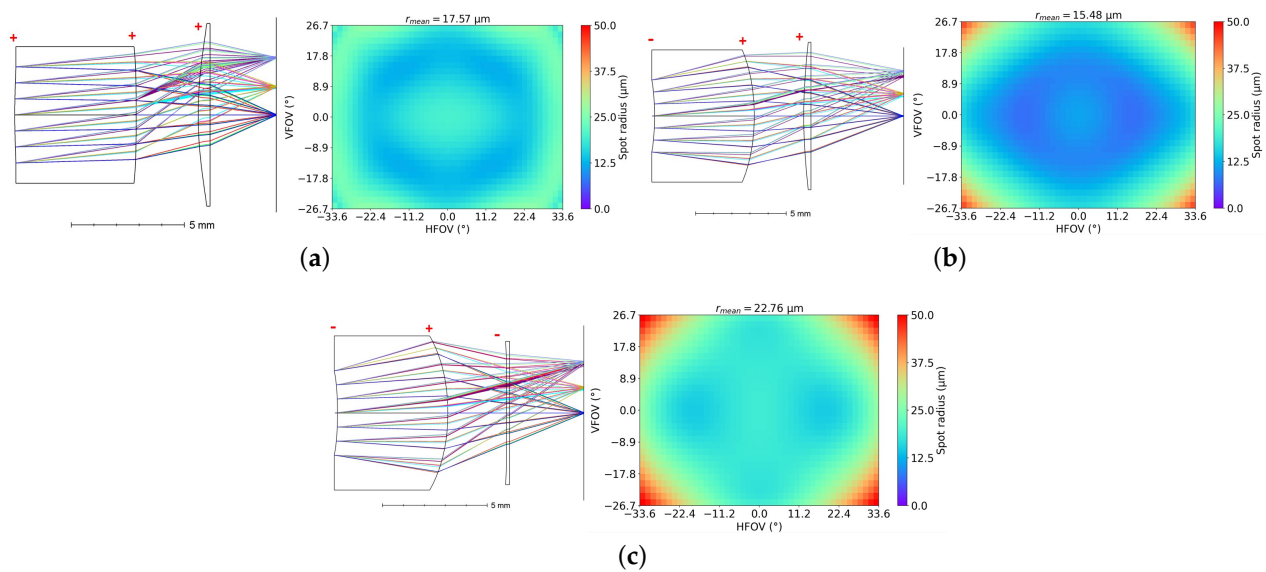


**Figure 12.** RMS spot radius field map using the same color map and layout of the best systems with an F-number of 1.2: (a) BSC(1) has a mean, minimum, and maximum RMS spot radius of  $r_{mean} = 17.57 \mu\text{m}$ ,  $r_{min} = 12.12 \mu\text{m}$ , and  $r_{max} = 26.31 \mu\text{m}$ ; (b) BSC(2) has a mean, minimum, and maximum RMS spot radius of  $r_{mean} = 15.48 \mu\text{m}$ ,  $r_{min} = 7.29 \mu\text{m}$ , and  $r_{max} = 44.83 \mu\text{m}$ ; (c) BSC(3) has a mean, minimum, and maximum RMS spot radius of  $r_{mean} = 22.76 \mu\text{m}$ ,  $r_{min} = 14.88 \mu\text{m}$ , and  $r_{max} = 51.17 \mu\text{m}$  with an F-number of 1.2.

After manually optimizing the three best systems, we obtained the three optimized systems shown in Figure 13. Figure 14 depicts the reference system and the RMS spot radius field maps of the three optimized systems normalized on the same color map. We can see that the optimization of BSC(1) did not lead to a good system, as it had a mean RMS spot radius of  $20.15 \mu\text{m}$ , which was widely superior to the mean RMS (equal to  $7.62 \mu\text{m}$ ) spot radius of the reference system. Thus, combining a front convex–convex thick lens followed by a convergent lens was not a good solution, as it only used convex surfaces; the system could not be corrected from the Petzval curvature and, thus, the field curvature. By contrast, the systems resulting from the optimization of BSC(2) and BSC(3) had a slightly better optical quality than the reference system, as they had mean RMS spot radii of  $6.75 \mu\text{m}$  and  $7.26 \mu\text{m}$ , respectively. It is interesting to note that we were able to design a convergent–divergent system (optimized BSC(3)) with better optical quality than the reference design. We enhanced the optical quality for the configuration of the same system, with mean RMS spot radii of  $7.27 \mu\text{m}$  and  $7.71 \mu\text{m}$  for the designed and reference systems, respectively (see Figure 14a). The improvement was relatively low, because the reference system was already diffraction-limited. Thus, we wanted to compare our two designed systems in more detail, especially looking at the effect of using a divergent lens in a two-lens system. Firstly, we looked at the X-axis and Y-axis focal lengths of the convergent front lens. We specified the axis of the focal length as we worked with freeform surfaces. Thus, the X-axis and Y-axis focal lengths were not necessarily equal. The X-axis and Y-axis focal lengths of the front lens of the optimized BSC(2) were equal to  $7.51 \text{ mm}$  and  $8.22 \text{ mm}$ . The aperture of the front lens was equal to the aperture of the system, as the pupil of the system was the first surface of the front lens, so it equalled  $4.75 \text{ mm}$ , leading to local F-numbers of  $1.58$  and  $1.73$  for the front lens along the X-axis and Y-axis. In this configuration, we used only convergent lenses that increased the F-number of the front lens compared to the F-number of the whole system, which equaled  $1.2$ . This effect helped to reduce the aberrations of the convergent lens, as increasing the F-number of a lens reduces the amplitude of its aberrations. By contrast, the X-axis and Y-axis focal lengths of the optimized BSC(3) were equal to  $4.96 \text{ mm}$  and  $5.29 \text{ mm}$  for an aperture value of  $4.42 \text{ mm}$ , leading to local F-numbers of  $1.12$  and  $1.19$  for the front lens along the X-axis and Y-axis, which were inferior to the

F-number of the whole system. Therefore, using a divergent lens decreased the F-number of the front lens, which means that a divergent lens may not be suitable for systems with a low F-number.

Secondly, we wanted to see if the divergent field-flattener lens helped to better correct the field curvature of the system. First, we needed to take a look at the layout of configuration 2, illustrated in Figure 12. We could see that the front lens was an inverse thick meniscus known to correct the aberrations of wide FOV systems, particularly the field curvature and, thus, the Petzval curvature [32]. Therefore, it was interesting to compare both field curvature corrections, to see if using only an inverse thick meniscus was sufficient or if it was necessary to use both: an inverse thick meniscus and a divergent field-flattener lens. To compare both configurations, we looked at the value of  $Z_4$ , the Zernike polynomial corresponding to the defocus and field curvature of the system. To this end, we defocused both systems, to obtain the best spot for the on-axis field, so as to compare both field curvatures equally. In doing so, the field curvature was no longer compensated for by the best focus of the system, and we removed, at the same time, the defocus contribution in  $Z_4$ . For configurations 2 and 3, the field curvature was the primary aberration in both cases, as it represented 88% and 60% of the total RMS wavefront error for configurations 2 and 3. Therefore, the divergent field-flattener lens was the better solution to correct the field curvature for this system. However, it reduced the local F-number of the front lens, resulting in a worse performance than the case of an inverse thick front meniscus followed by a convergent silicon lens. Therefore, an inverse thick meniscus is sufficient to handle the field curvature of the system. Using a divergent field flattener is unnecessary, and it decreases the final optical quality, by decreasing the local F-number of the inverse thick meniscus, thereby increasing its aberrations.

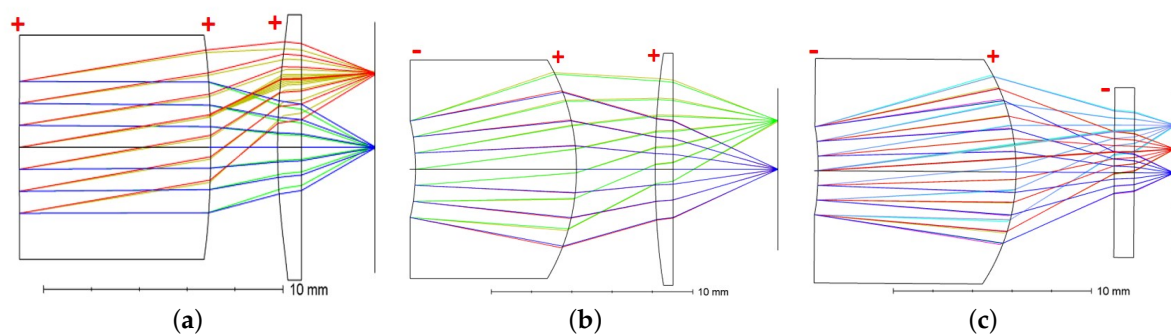


**Figure 13.** Layout of the optimized systems with an F-number of 1.2: (a) configuration 1; (b) configuration 2; (c) configuration 3.

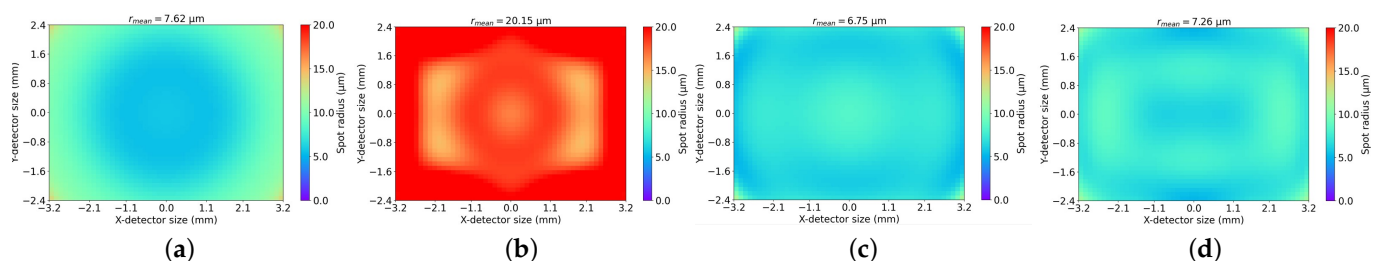


**Figure 14.** RMS spot radius field map: (a) reference system has a mean, minimum, and maximum RMS spot radius of  $r_{mean} = 7.62 \mu\text{m}$ ,  $r_{min} = 5.45 \mu\text{m}$ , and  $r_{max} = 13.32 \mu\text{m}$ ; (b) configuration 1 has a mean, minimum, and maximum RMS spot radius of  $r_{mean} = 20.15 \mu\text{m}$ ,  $r_{min} = 14.74 \mu\text{m}$ , and  $r_{max} = 34.91 \mu\text{m}$ ; (c) configuration 2 has a mean, minimum, and maximum RMS spot radius of  $r_{mean} = 6.75 \mu\text{m}$ ,  $r_{min} = 5.18 \mu\text{m}$ , and  $r_{max} = 11.49 \mu\text{m}$ ; (d) configuration 3 has a mean, minimum, and maximum RMS spot radius of  $r_{mean} = 7.26 \mu\text{m}$ ,  $r_{min} = 5.21 \mu\text{m}$ , and  $r_{max} = 11.23 \mu\text{m}$ .

#### 2.4.4. Study of a Monochromatic Two-Lens Infrared System with an Aperture of F/0.9

In this study, we wanted to take full advantage of our global approach and of the correction of the useful rectangular FOV, to design a fast freeform system with an F-number of 0.9. Using the automated method, we obtained the configuration map in Figure 15. We observed the same consequences as the second study: a reduction in the number of designed systems and their optical quality. These observations were unsurprising, as we further reduced the F-number while keeping the FOV of the systems constant. The repartition of the configuration differed slightly from before, as we had two principles and one marginal configuration. Figure 16 shows that the global approach did not design a system with a front convergent lens and a divergent field-flattener lens as the reference system for this F-number, which shows that it is unsuitable to use a divergent field-flattener lens in a two-lens system when the F-number becomes too low. Thus, by looking at the three RMS spot radius field maps of the best system of each configuration, illustrated in Figure 16, we can remark that the difference in optical quality between the BSC of each configuration was higher than for the previous studies. Indeed, BSC(1) had a mean RMS spot radius of 16.97  $\mu\text{m}$  and was two times better than BSC(3), which had a mean RMS spot radius of 34.2  $\mu\text{m}$ .

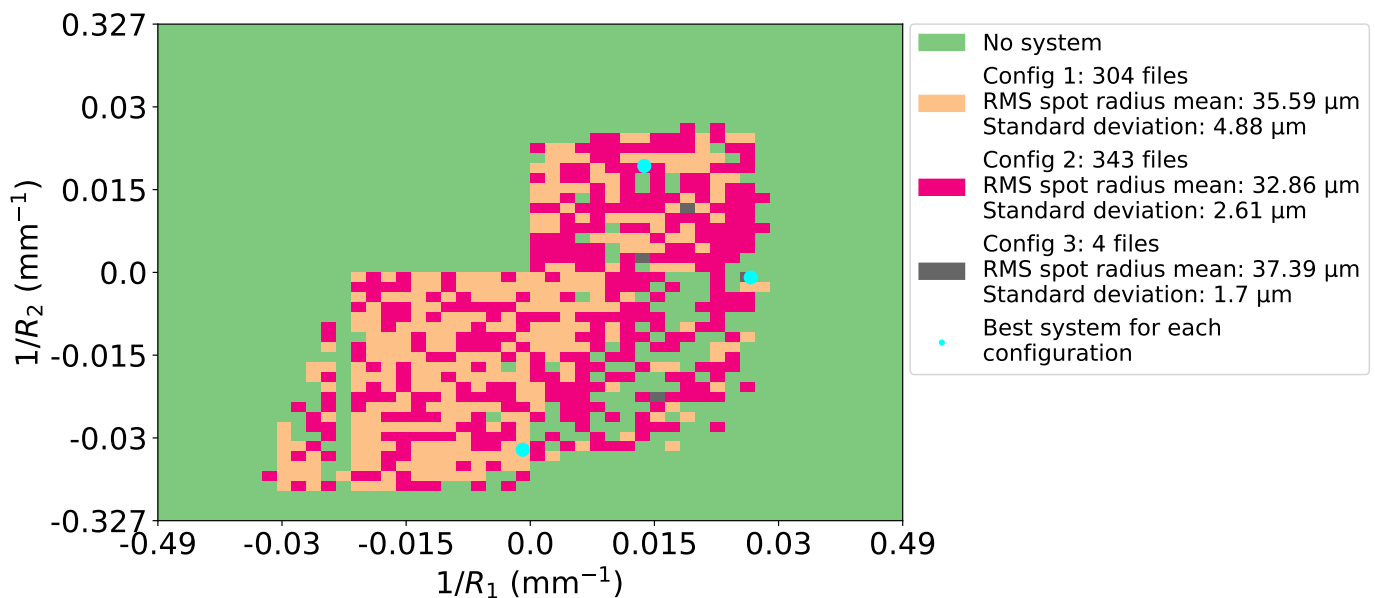


**Figure 15.** Map of the configurations found for a monochromatic two-lens infrared system with an aperture of F/0.9 according to  $1/R_1$  and  $1/R_2$  ( $r_{\text{Airy}} = 10.37 \mu\text{m}$ ).

After manual optimization, we obtained the three RMS spot radius field maps and layouts shown in Figure 17. By comparing the layouts of Figure 16 and those of Figure 17, we can see that configurations 1 and 2 kept the same configuration shapes, contrary to configuration 3, which completely changed its shape to reach the same shape as configuration 2. Finally, we had two different configurations. Configuration 1 reached a significantly better optical quality, with a mean RMS spot radius of 6.96  $\mu\text{m}$ , than configurations 2 and 3, with RMS spot radii of 22.03  $\mu\text{m}$  and 25.56  $\mu\text{m}$ , respectively. It is interesting to understand which aberration causes the degradation of the optical quality between both configurations. For configuration 1, we found that the primary aberration for its field with the worst optical quality was the coma, with a contribution of 80% to the total RMS wavefront error. In this configuration, the field curvature contribution was ten times lower than the coma contribution, which was about 8%. This demonstrated that the inverse thick meniscus allowed for a significant correction of the field curvature. Configuration 2 did not use an inverse thick meniscus or a field-flattener lens to correct the field curvature. It used a third mechanism instead, which uses astigmatism to correct the field curvature of a system [32]. This mechanism led to a field curvature contribution of 18% to the total RMS wavefront

error. However, an astigmatism at  $45^\circ$  contributed to 81% of the total RMS wavefront errors, leading to a non-diffraction-limited system. Thus, the astigmatism limited the optical quality of the system. This observation demonstrates that using astigmatism to correct field curvature for fast and wide FOV with two air-spaced lenses is not the best solution. Therefore, the preferred mechanism is using an inverse thick meniscus to correct the field curvature for this type of system, which is not obvious, as optical designers often use a field-flattener lens to correct this aberration.

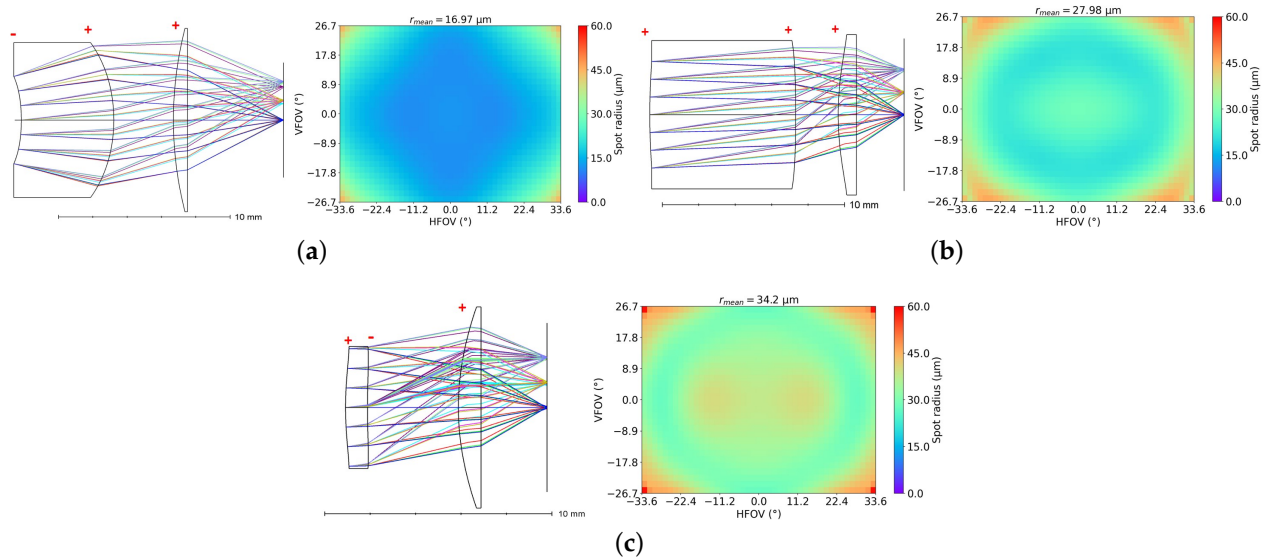


**Figure 16.** RMS spot radius field map on the same color map and layout of the best systems with an F-number of 0.9: (a) BSC(1) has a mean, minimum, and maximum RMS spot radius of  $r_{mean} = 16.97 \mu\text{m}$ ,  $r_{min} = 11.27 \mu\text{m}$ , and  $r_{max} = 44.01 \mu\text{m}$ ; (b) BSC(2) has a mean, minimum, and maximum RMS spot radius of  $r_{mean} = 27.98 \mu\text{m}$ ,  $r_{min} = 20.85 \mu\text{m}$ , and  $r_{max} = 46.03 \mu\text{m}$ ; (c) BSC(3) has a mean, minimum, and maximum RMS spot radius of  $r_{mean} = 34.2 \mu\text{m}$ ,  $r_{min} = 27.35 \mu\text{m}$ , and  $r_{max} = 58.77 \mu\text{m}$ .

Finally, we selected the system of configuration 1 to be further optimized, resulting in the final freeform system, with the layout and RMS spot radius field depicted in Figure 18. Ultimately, the designed system had an F-number of 0.9, and it was very close to being diffraction-limited over the whole detector. Indeed, it had a mean RMS spot radius of  $9.9 \mu\text{m}$  for an Airy spot radius of  $10.98 \mu\text{m}$  for this aperture. This system comprised an inverse thick meniscus and a thin rear convergent lens. In the final system, the primary aberration was the field curvature, demonstrating that it is essential to correct this aberration for fast two-lens systems with wide FOV.

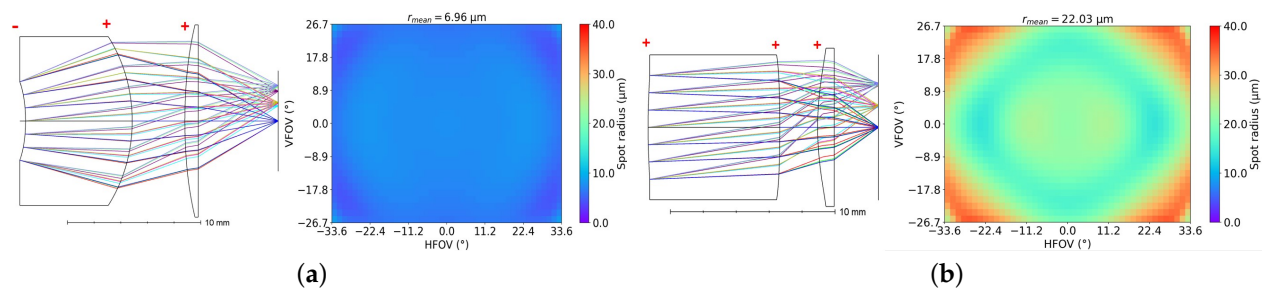


**Figure 17.** Cont.

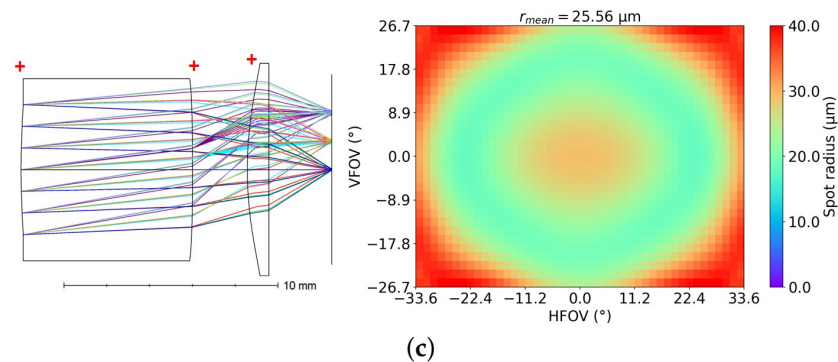


**Figure 17.** RMS spot radius field map on the same color map and layout of the optimized systems with an F-number of 0.9: (a) configuration 1 has a mean, minimum, and maximum RMS spot radius of  $r_{mean} = 6.96 \mu\text{m}$ ,  $r_{min} = 4.40 \mu\text{m}$ , and  $r_{max} = 8.47 \mu\text{m}$ ; (b) configuration 2 has a mean, minimum, and maximum RMS spot radius of  $r_{mean} = 22.03 \mu\text{m}$ ,  $r_{min} = 14.34 \mu\text{m}$ , and  $r_{max} = 35.38 \mu\text{m}$ ; (c) configuration 3 has a mean, minimum, and maximum RMS spot radius of  $r_{mean} = 25.56 \mu\text{m}$ ,  $r_{min} = 18.03 \mu\text{m}$ , and  $r_{max} = 40.31 \mu\text{m}$ .

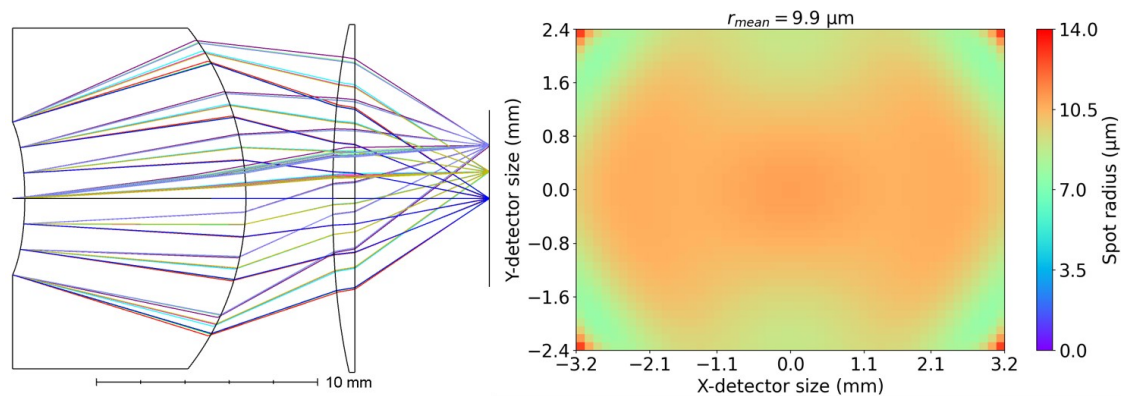


**Figure 18.** Layout and RMS spot radius field map of the final freeform system with an F-number of 0.9. The final system had a mean, minimum, and maximum RMS spot radius of  $r_{mean} = 9.9 \mu\text{m}$ ,  $r_{min} = 7.64 \mu\text{m}$ , and  $r_{max} = 12.80 \mu\text{m}$ .

### 2.5. Current Limitations of the Automated Method and Major Source of Error

We demonstrated in the previous sections the capabilities of the automated method, but we also need to discuss its limitations and a major source of error. The first limitation of the method is that it can only design systems with up to three unknown surfaces. This was not a limitation in our particular case, as we wanted to design systems with a maximum of three freeform surfaces. The second limitation is the computation time, which can be significant (several days) for complex optical problems (low F-number and wide FOV): this is due to automatic optimization in Zemax. Indeed, Zemax can run only four instances simultaneously. Thus, we can only optimize four systems simultaneously. To bypass this limitation, we intend to use a custom ray tracer in the future, which is a parallel processing algorithm. Using our ray tracing software, we estimate that the computation time will be, at most, one day for complex optical problems and a large set of initial settings.

Currently, the major source of error for the reliability of the method is the local algorithm used to optimize the different systems, which can become stuck in a bad local minimum. Nevertheless, our method runs optimization multiple times, beginning with slightly different starting points, which mitigates this problem. Therefore, the errors will only be outliers in the configuration map, and we will not have a loss of information.

## 3. Conclusions

In this article, we used our implementation of the SMS-3S-3D method to implement an automated method of exploring a merit function landscape of two-lens infrared freeform

systems. We demonstrated the ability of the method to scan the merit function of a freeform optical problem, finding different relevant starting configurations for further optimization. The method aims to help the optical designer to pick the best starting system for its optical problem, drastically reducing its effort in this trial-and-error process. We proved that our automatic method finds the same starting configuration used by an experienced optical designer. This configuration uses a divergent field-flattener lens to correct the field curvature of the system. We also showed that this starting configuration, based on the experience of the designer, is quite difficult to find without experience, as it was only found two times via the automatic method. The automatic method also found another suitable configuration, using an inverse thick meniscus and a convergent rear lens, as the inverse thick meniscus allows for the correction of the field curvature. We compared both configurations, showing that the divergent field-flattener lens is better at correcting the field curvature. However, it increases the local F-number of the front lens, making its use unsuitable for fast systems. Indeed, by applying our automatic method to design a system with a faster F-number of 0.9, we found that the best configuration combines a front inverse thick meniscus followed by a convergent silicon lens. This illustrates that the inverse thick meniscus can attenuate the field curvature and is, thus, a preferred solution as a front lens for systems answering a SWaP problem. The designed freeform infrared system is very close to the diffraction limit over its wide FOV. Demonstrators should, however, be made, to verify that the decrease in the F-number and the use of three freeform surfaces will not drastically increase the cost of the system, which is an important criterion, for example, in automotive applications. This article also illustrated the benefits of using freeform surfaces in dioptric systems, to correct the useful FOV defined by a rectangular detector and to enhance the optical performance of the system.

**Author Contributions:** Conceptualization, T.M., J.-B.V. and G.D.; methodology, T.M., J.-B.V. and G.D.; software, T.M. and J.-B.V.; validation, J.-B.V. and G.D.; investigation, T.M.; writing—original draft preparation, T.M.; writing—review and editing, T.M., G.D., J.-B.V., A.D., F.C. and E.T.; supervision, G.D., J.-B.V., A.D., F.C. and E.T.; project administration, G.D. All authors have read and agreed to the published version of this manuscript.

**Funding:** The authors acknowledge the National Technology Research Association (ANRT), Safran Electronics & Defense, Lynred, and ONERA for funding this research program.

**Institutional Review Board Statement:** Not applicable.

**Informed Consent Statement:** Not applicable.

**Data Availability Statement:** The data underlying the results presented in this paper are not publicly available at this time, but may be obtained from the authors upon reasonable request.

**Conflicts of Interest:** The authors declare no conflict of interest.

## References

1. Plummer, W.T. Unusual optics of the Polaroid SX-70 Land camera. *Appl. Opt.* **1982**, *21*, 196. [[CrossRef](#)] [[PubMed](#)]
2. Rolland, J.P.; Davies, M.A.; Suleski, T.J.; Evans, C.; Bauer, A.; Lambropoulos, J.C.; Falaggis, K. Freeform optics for imaging. *Optica* **2021**, *8*, 161. [[CrossRef](#)]
3. Schiesser, E.M.; Bauer, A.; Rolland, J.P. Effect of freeform surfaces on the volume and performance of unobscured three mirror imagers in comparison with off-axis rotationally symmetric polynomials. *Opt. Express* **2019**, *27*, 21750. [[CrossRef](#)] [[PubMed](#)]
4. Buquet, J.; Parent, J.; Lalonde, J.F.; Thibault, S. Challenges using data-driven methods and deep learning in optical engineering. In *Proceedings of the Current Developments in Lens Design and Optical Engineering XXIII*; Padilla-Vivanco, A., Johnson, R.B., Mahajan, V.N., Thibault, S., Eds.; SPIE: San Diego, CA, USA, 2022; p. 17. [[CrossRef](#)]
5. Thibault, S.; Buquet, J.; Coté, G.; Lalonde, J.F. Recent progress of AI in lens design (Conference Presentation). In *Proceedings of the Optical Design and Testing XII*; Wu, R., Wang, Y., Kidger, T.E., Eds.; SPIE, China, 2022; p. 23. [[CrossRef](#)]
6. Nie, Y.; Zhang, J.; Su, R.; Ottevaere, H. Freeform optical system design with differentiable three-dimensional ray tracing and unsupervised learning. *Opt. Express* **2023**, *31*, 7450. [[CrossRef](#)] [[PubMed](#)]
7. Yang, T.; Cheng, D.; Wang, Y. Direct generation of starting points for freeform off-axis three-mirror imaging system design using neural network based deep-learning. *Opt. Express* **2019**, *27*, 17228. [[CrossRef](#)] [[PubMed](#)]

8. Wang, L. *Advances in the Simultaneous Multiple Surface Optical Design Method for Imaging and Non-Imaging Applications*; Universidad Politécnica de Madrid: Madrid, Spain, 2012.
9. Nikolić, M. SMS for Imaging Systems Using Free-Forms. Ph.D. Thesis, Universidad Politécnica de Madrid, Madrid, Spain, 2017. [[CrossRef](#)]
10. Miñano, J.C.; Benítez, P.; Lin, W.; Infante, J.; Muñoz, F.; Santamaría, A. An application of the SMS method for imaging designs. *Opt. Express* **2009**, *17*, 24036. [[CrossRef](#)] [[PubMed](#)]
11. Miñano, J.C.; Benítez, P.; Narasimhan, B. Freeform aplanatic systems as a limiting case of SMS. *Opt. Express* **2016**, *24*, 13173. [[CrossRef](#)] [[PubMed](#)]
12. Miñano, J.C.; González, J.C. New method of design of nonimaging concentrators. *Appl. Opt.* **1992**, *31*, 3051. [[CrossRef](#)] [[PubMed](#)]
13. Muñoz, F.; Infante Herrero, J.M.; Benítez, P.; Miñano, J.C.; Lin, W.; Vilaplana, J.; Biot, G.; de la Fuente, M. Novel Fast Catadioptric Objective with Wide Field of View; In *Proceedings of the SPIE NanoScience + Engineering*; SPIE: San Diego, CA, USA, 2010; p. 77800T. [[CrossRef](#)]
14. Lin, W.; Benítez, P.; Miñano, J.C.; Infante, J.M.; Biot, G.; de la Fuente, M. SMS-based optimization strategy for ultra-compact SWIR telephoto lens design. *Opt. Express* **2012**, *20*, 9726. [[CrossRef](#)] [[PubMed](#)]
15. Mohedano, R.; Benítez, P.; Nikolic, M.; Chaves, J.; Miñano, J.C.; Grabovickic, D.; Buljan, M.; Zamora, P. Notes on the design of free-form optics. In *Proceedings of the AI and Optical Data Sciences*; Kitayama, K.i., Jalali, B., Eds.; SPIE: San Francisco, CA, USA, 2020; p. 3. [[CrossRef](#)]
16. Miñano, J.C.; Benítez, P.; Lin, W.; Muñoz, F.; Infante, J.; Santamaría, A. *Overview of the SMS Design Method Applied to Imaging Optics*; In *Proceedings of the SPIE Optical Engineering + Applications*; SPIE: San Diego, CA, USA, 2009; p. 74290C. [[CrossRef](#)]
17. Lin, W.; Benítez, P.; Miñano, J.C.; Infante, J.; Biot, G. *Progress in the SMS Design Method for Imaging Optics*; In *Proceedings of the SPIE Optical Engineering + Applications*; SPIE: San Diego, CA, USA, 2011; p. 81280F. [[CrossRef](#)]
18. Benitez, P. Freeform optics design. In *Proceedings of the Optical Design and Engineering VIII*; Babington, J., Fuchs, U., Mazuray, L., Eds.; SPIE: Noáin, Spain, 2021; p. 501. [[CrossRef](#)]
19. Benitez, P. Simultaneous multiple surface optical design method in three dimensions. *Opt. Eng.* **2004**, *43*, 1489. [[CrossRef](#)]
20. Yang, T.; Zhu, J.; Wu, X.; Jin, G. Direct design of freeform surfaces and freeform imaging systems with a point-by-point three-dimensional construction-iteration method. *Opt. Express* **2015**, *23*, 10233–10246. [[CrossRef](#)] [[PubMed](#)]
21. Yang, T.; Zhu, J.; Hou, W.; Jin, G. Design method of freeform off-axis reflective imaging systems with a direct construction process. *Opt. Express* **2014**, *22*, 9193–9205. [[CrossRef](#)] [[PubMed](#)]
22. Volatier, J.B.; Mendiña-Fernández, Á.; Erhard, M. Generalization of differential ray tracing by automatic differentiation of computational graphs. *J. Opt. Soc. Am. A* **2017**, *34*, 1146. [[CrossRef](#)] [[PubMed](#)]
23. Volatier, J.B.; Druart, G. Differential method for freeform optics applied to two-mirror off-axis telescope design. *Opt. Lett.* **2019**, *44*, 1174. [[CrossRef](#)] [[PubMed](#)]
24. Duerr, F.; Thienpont, H. Optical design of first time right imaging systems. In *Proceedings of the Optical Design and Testing XII*; Wu, R., Wang, Y., Kidger, T.E., Eds.; SPIE: Beijing, China, 2022; p. 27. [[CrossRef](#)]
25. Nie, Y.; Shafer, D.R.; Ottevaere, H.; Thienpont, H.; Duerr, F. Automated freeform imaging system design with generalized ray tracing and simultaneous multi-surface analytic calculation. *Opt. Express* **2021**, *29*, 17227. [[CrossRef](#)] [[PubMed](#)]
26. Duerr, F.; Thienpont, H. Freeform imaging systems: Fermat's principle unlocks "first time right" design. *Light Sci. Appl.* **2021**, *10*, 95. [[CrossRef](#)] [[PubMed](#)]
27. Druart, G.; Reux, V.; Calvez, L.; Zhang, X.H.; de la Barrière, F.; Volatier, J.B.; Tartas, E.; Proux, R. Evaluation of the potential of high index chalcogenide lenses for automotive applications. In *Proceedings of the Advanced Optics for Imaging Applications: UV through LWIR VII*; Marasco, P.L., Sanghera, J.S., Vizgaitis, J.N., Eds.; SPIE: Orlando, FL, USA, 2022; p. 16. [[CrossRef](#)]
28. Bigwood, C.; Wood, A. "It's Only Two Lenses in a Tube: How Complicated Can it Be?"; In *Proceedings of the SPIE Defense, Security, and Sensing*; SPIE: Orlando, Florida, USA, 2009; p. 72980Z.
29. Schuster, N.; Franks, J. *Two-Lens Designs for Modern Uncooled and Cooled IR Imaging Devices*; In *Proceedings of the SPIE Defense, Security, and Sensing*; SPIE: Orlando, Florida, USA, 2009; p. 889604. . 10.1117/12.2028716. [[CrossRef](#)]
30. Duerr, F.; Meuret, Y.; Thienpont, H. Potential benefits of free-form optics in on-axis imaging applications with high aspect ratio. *Opt. Express* **2013**, *21*, 31072. [[CrossRef](#)] [[PubMed](#)]
31. Duerr, F.; Benítez, P.; Miñano, J.C.; Meuret, Y.; Thienpont, H. *Analytic Free-Form Lens Design for Imaging Applications with High Aspect Ratio*; In *Proceedings of SPIE Optical Engineering + Applications*; SPIE: San Diego, CA, USA, 2012; p. 848609. [[CrossRef](#)]
32. Sasián, J. Field Curvature Aberration; In *Proceedings of the International Optical Design Conference, Kohala Coast, HI, USA, 23–26 June 2014*; p. 929322. [[CrossRef](#)]

**Disclaimer/Publisher's Note:** The statements, opinions and data contained in all publications are solely those of the individual author(s) and contributor(s) and not of MDPI and/or the editor(s). MDPI and/or the editor(s) disclaim responsibility for any injury to people or property resulting from any ideas, methods, instructions or products referred to in the content.